



HAL
open science

The shallow three-dimensional structure of Volcán de Colima revealed by ambient seismic noise tomography

Raphael S.M. de Plaen, Aurélien Mordret, Raul Arámbula-Mendoza, Dulce Vargas-Bracamontes, Victor Hugo Márquez-Ramírez, Thomas Lecocq, Carlos Ariel Ramírez Vázquez, Miguel González Amezcua

► To cite this version:

Raphael S.M. de Plaen, Aurélien Mordret, Raul Arámbula-Mendoza, Dulce Vargas-Bracamontes, Victor Hugo Márquez-Ramírez, et al.. The shallow three-dimensional structure of Volcán de Colima revealed by ambient seismic noise tomography. *Journal of Volcanology and Geothermal Research*, 2022, 428, pp.107578. 10.1016/j.jvolgeores.2022.107578 . insu-03877706

HAL Id: insu-03877706

<https://insu.hal.science/insu-03877706>

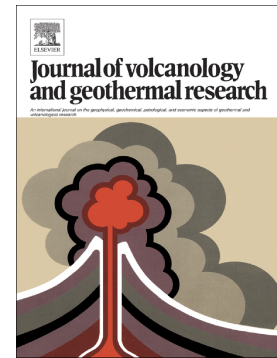
Submitted on 4 May 2023

HAL is a multi-disciplinary open access archive for the deposit and dissemination of scientific research documents, whether they are published or not. The documents may come from teaching and research institutions in France or abroad, or from public or private research centers.

L'archive ouverte pluridisciplinaire **HAL**, est destinée au dépôt et à la diffusion de documents scientifiques de niveau recherche, publiés ou non, émanant des établissements d'enseignement et de recherche français ou étrangers, des laboratoires publics ou privés.

The shallow three-dimensional structure of Volcán de Colima revealed by ambient seismic noise tomography

Raphael S.M. De Plaen, Aurélien Mordret, Raul Arámbula-Mendoza, Dulce Vargas-Bracamontes, Victor Hugo Márquez-Ramírez, Thomas Lecocq, Carlos Ariel Ramírez Vázquez, Miguel González Amezcuca



PII: S0377-0273(22)00109-3

DOI: <https://doi.org/10.1016/j.jvolgeores.2022.107578>

Reference: VOLGEO 107578

To appear in: *Journal of Volcanology and Geothermal Research*

Received date: 23 September 2021

Revised date: 21 April 2022

Accepted date: 15 May 2022

Please cite this article as: R.S.M. De Plaen, A. Mordret, R. Arámbula-Mendoza, et al., The shallow three-dimensional structure of Volcán de Colima revealed by ambient seismic noise tomography, *Journal of Volcanology and Geothermal Research* (2021), <https://doi.org/10.1016/j.jvolgeores.2022.107578>

This is a PDF file of an article that has undergone enhancements after acceptance, such as the addition of a cover page and metadata, and formatting for readability, but it is not yet the definitive version of record. This version will undergo additional copyediting, typesetting and review before it is published in its final form, but we are providing this version to give early visibility of the article. Please note that, during the production process, errors may be discovered which could affect the content, and all legal disclaimers that apply to the journal pertain.

The shallow three-dimensional structure of Volcán de Colima revealed by ambient seismic noise tomography

Raphael S.M. De Plaen^{1,2}, Aurélien Mordret³, Raul Arámbula-Mendoza⁴, Dulce Vargas-Bracamontes⁴, Victor Hugo Márquez-Ramírez¹, Thomas Lecocq², Carlos Ariel Ramírez Vázquez⁴, Miguel González Amezcu⁴

¹*Centro de Geociencias, Universidad Nacional Autónoma de México, Campus Juriquilla, Querétaro, Mexico*

²*Royal Observatory of Belgium, Seismology-Gravimetry, Avenue Circulaire 3, 1180 Uccle, Belgium*

³*Institut des Sciences de la Terre, Université Grenoble Alpes, Grenoble, France*

⁴*Centro Universitario de Estudios Vulcanológicos (CUEV), Universidad de Colima, Colima, Mexico*

Abstract

Volcán de Colima is one of the most active volcanoes in North America. Even so, it has a poorly constrained upper crustal structure. Here, we present the highest-resolution three-dimensional shear-wave velocity tomography to date of the volcano.

We measured group velocity dispersion curves of Rayleigh and Love waves extracted from ambient seismic noise recorded on the Colima Volcanic Complex and regionalised them into 2-D velocity maps. Those were then locally inverted using a neighbourhood algorithm to obtain accurate shear-velocity models down to 4 km below sea level. The resulting three-dimensional shear wave velocity model gives us a new insight into the internal structure of the volcano to specifically better understand the shallow magma storage and magmatic plumbing system and, in turn, how it can be placed in a wider geotectonic context.

Our results highlight a network of deeply rooted NE-SW low velocity zones oriented along a local fault system. The southward orientation of this low-velocity anomaly also roughly aligns with the north-south trend of the volcanoes that compose the quaternary Colima Volcanic Complex and could be associated with the gradual trenchward shift of the magmatic front of the volcanic complex dating from the formation of the Cántaro Volcano. The low-velocity anomaly overlaps a negative radial anisotropy indicating that magma follows vertically oriented structures, such as interfingering dikes or faults and cracks with a substantial vertical component.

The low velocity anomaly under Volcán de Colima contrasts with a distinct high-velocity anomaly under Nevado de Colima that highlights the difference

between the former active system, filled with solidified dikes and sills, and the current one, associated with a network of fluid-filled dikes.

Keywords: ambient noise tomography, volcano, magmatic plumbing system

Journal Pre-proof

1. Introduction

When studying active volcanoes, understanding the mechanisms behind the emplacement and ascent of the magma inside the crust can provide significant insight into the expected behavior of a volcano. The magmatic processes in the volcanic plumbing system directly impact the size and the type of an eruption, motivating the careful determination of the geometry of fluid pathways and magma reservoirs. High resolution imaging of the structure of a volcano offers a way to infer its geological history which, in turn, can be placed in a wider geotectonic context.

Volcán de Colima, also referred to as Fuego de Colima, is one of the most active volcanoes in Mexico and in North America with eruptions and sector collapses posing a high risk for more than 500,000 people in surrounding cities (Capra et al., 2015; Norini et al., 2019). The volcano is located in western Mexico (Figure 1), at the exceptionally complex conjunction of tectonic processes (e.g., Ferrari et al., 2012). While it has the highest probability of a VEI ≥ 4 eruption in Mexico within the next 20 years (Mendoza-Rosas and De la Cruz-Reyes, 2008), Volcán de Colima has gone through various styles of activity throughout its eruptive history ranging from less-intense effusive and explosive periods to explosive sub-Plinian to Plinian eruptions. The last two sub-Plinian to Plinian eruptions, both classified as VEI = 4, occurred in 1818 and in 1913. The most recent activity has been characterized by an alternation of multiple vulcanian eruptions, lava flows, dome formations, and dome collapses (Reyes-Dávila et al., 2016). However, a large event such as the 1913 eruption would now pose a severe risk for the 500,000 people living in the vicinity of the volcano (Saucedo et al., 2010).

Fully understanding the structural control on the evolution of the volcanic complex and its activity requires an accurate insight into the relationship between the regional tectonics, the magmatic system and the weak basement. Such information can be extracted by using seismic tomography to analyze the seismic velocity structure of the volcano. Seismic tomography is a powerful tool in volcanic environments that can rely on earthquakes or ambient seismic noise. The crustal structure beneath the Colima volcanic complex (CVC) has been studied and imaged using both source types and different strategies with distinct performances at different depths.

A series of body-wave tomographic studies used teleseisms (Yang et al., 2009), regional (Ochoa-Chávez et al., 2016), and local earthquakes (Sychev et al., 2019) to image the crust down to the upper mantle. Besides the velocity structure under the CVC, Sychev (2019) notably estimated the seismic attenuation in the region.

The S-wave velocity structure of the CVC has also been imaged using ambient seismic noise at regional scale by Castellanos et al. (2018) and Spica et al. (2017). The main advantage of using ambient noise instead of local and regional earthquakes is that the noise tomography is not limited by the spatial and/or temporal distribution of seismicity. Nevertheless, those regional models offer a low resolution under volcán de Colima. Escudero and Bandy (2017) worked at local scale instead to produce

ambient noise Rayleigh-wave group velocity maps at 3 and 5s, but did not perform a full depth inversion.

Most seismic tomographies of Volcán de Colima resulted in regional models with poor resolution under the edifice, especially in the upper crust. As a result, the structure and geometry of plumbing system in the upper 10 km remains poorly defined, with some speculation of a shallow magma chamber at ~7km depth that still has to be imaged (e.g., Spica et al., 2017).

Here, we address this short-coming and specifically study the upper crust by performing a joint inversion of Rayleigh and Love wave group velocity dispersion curves to assess both the shear wave velocity and radial anisotropy structure under Volcán de Colima at a local scale.

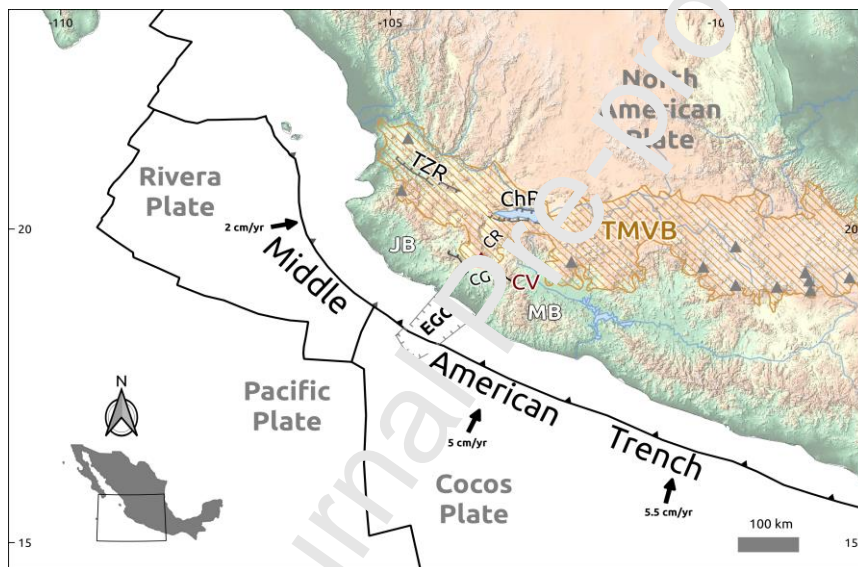


Figure 1. Tectonic setting of Western Mexico: the Jalisco block (JB), the Michoacán block (MB), the Tepec-Zacoalco Rift (TZR), the Chapala Rift (ChR), the Colima Rift (CR), El Gordo Graben (EGG), and the Colima Graben (CG). The Pliocene-Quaternary Trans-Mexican Volcanic Belt (TMVB) comprises the area within the orange hatched area. The gray triangles are volcanoes, the red triangle shows the location of Volcán de Colima. The inset shows the regional location of the map in Mexico.

2. Geological setting

The volcán de Colima is part of the Colima Volcanic Complex (CVC) consisting of three N-S aligned calc-alkaline andesitic stratovolcanoes, along with a number of monogenetic scoria cones of presumably Pleistocene age (Luhr and Carmichael, 1980; Robin et al., 1987): the now extinct and strongly eroded El Cántaro (3,860 m), the large Nevado de Colima (4,340 m), and Volcán de Colima (3,860 m) (Figure 2). The CVC is located along the Middle America subduction zone and, more notably, near one of the world's most complex convergent margins in the world. The subduction presumably controlled the development of the Trans-Mexican Volcanic Belt (TMVB), a ~1000-kilometer-long continental volcanic arc with a peculiar lack of parallelism with the Middle America trench (Figure 1).

Here the Rivera and the Cocos plates are subducting under the North American plate with different ages, compositions, convergence vectors, and dipping angles while likely being separated by a trench-orthogonal tear starting just north of Volcán de Colima. This gap between the two subducting plates likely played a critical role in the formation of the CVC (Ferrari, 2004; Yang et al., 2009). Within the study area, the subduction is also responsible for the fragmentation of the Jalisco and the Michoacán blocks from the overriding continental North American plate. Those distinct geological units are separated by extensional corridors called Tepic–Zacoalco rift (TZR) in a NW–SE direction, and Colima rift (CR) in a N-S orientation (Ferrari et al., 2012; Ferrari and Rosas-Elguera, 2000; Yang et al., 2009). The TZR and the CR connect to the Chapala-Tula rifts (CTR) to form the Guadalajara triple junction (Allan, 1986; Ferrari and Rosas-Elguera, 2000; Luhr et al., 1985).

Besides those well-known tectonic features, the Tamazula fault (TF) has a more disputed origin and influence that has been described in the literature by two contrasting hypotheses. On the one hand, it has been interpreted as a major NE-SW-striking regional fault cutting through the CR and the CVC and extending for more than 160 km from the Michoacán block to the Manzanillo Bay (Cortés et al., 2010; Garduño-Monroy et al., 1998; Rosas-Elguera et al., 1996). The system mostly includes normal faults generating a NW-SE-trending extensional activity, cutting through the CVC and potentially at the origin of the many past episodes of collapse with preferred direction toward the S and SE (Garduño-Monroy et al., 1998) and toward the SW (Cortés et al., 2010). The current activity of the TF has been inferred from the alignment of crustal earthquakes in the Manzanillo area and along parallel crustal structures (e.g., Domínguez et al., 2001; Núñez-Cornú and Sánchez-Mora, 1999; Pacheco et al., 2003; Zobin et al., 2002). The intersection of the fault system with the CR is interpreted as a zone of weakened crust which, in turn, allowed the development of the volcanic complex. Hence, the occurrence of magma migration along the TF is reflected in the NE-SW alignment of Volcán de Colima and the Volcancito parasitic cone.

On the other hand, Norini et al. (2019, 2010) offer a distinct interpretation and associate several fault scarps previously associated to the TF to a 30 km E-W-trending fault system intersecting the CVC across the eastern and western flanks of Nevado de Colima. This unnamed system is characterized by normal kinematics and N-S extension. Along with the TF, they attribute this local volcano- tectonic structure to

the southward gravitational spreading of the volcanic complex due to the loading of the volcanic edifice over the weak sedimentary fill of the CR gently dipping to the south.

These two distinct explanations on the origin of the TF system eventually impact the overall interpretation of the structural architecture and evolutionary mechanisms of the CVC.

3. Ambient noise tomography

The ambient noise tomography was implemented in four main steps. The first involved the computation of the cross-correlations functions between pairs of stations for combinations of vertical, radial and transverse components (e.g., ZZ, RR, TT). The frequency dependent group travel times were then measured to later be used to construct the 2D group velocity maps at different periods. Finally, the depth structure was revealed by taking advantage of the regionalized dispersion curves for local 1D shear velocity models in every cell of a grid using a neighborhood algorithm.

3.1 Seismic data and computation of cross-correlations

Data

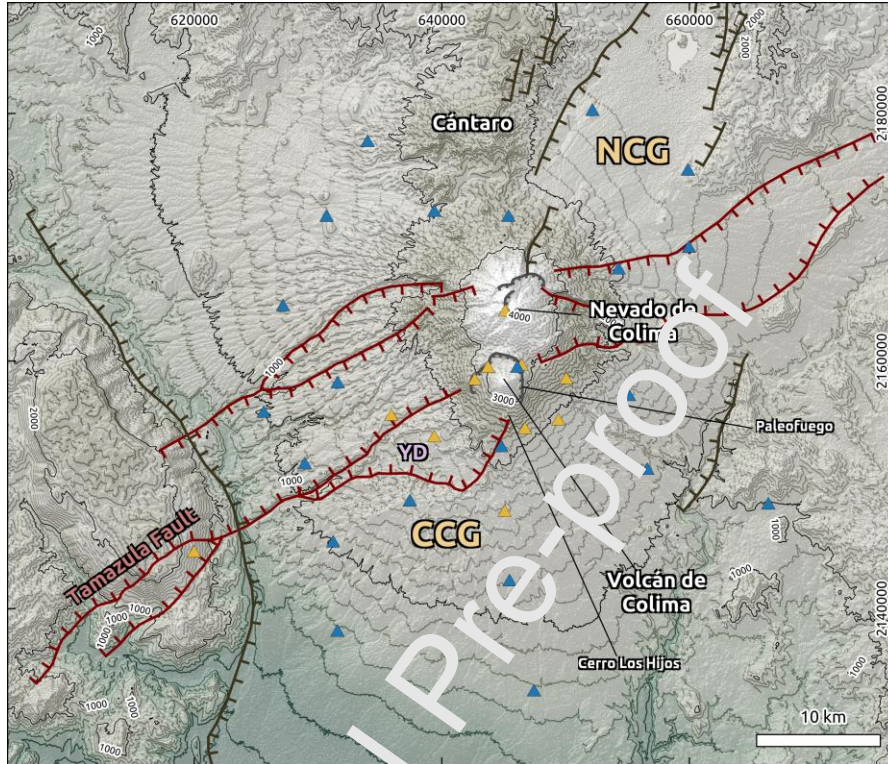


Figure 2. Location map for the stations from CODEX (blue triangles) and RESCO (orange triangle) used in this study. The Cántaro, Nevado de Colima, and Volcán de Colima form the Colima volcanic complex. The red line corresponds to Tamazula fault. YD is the Yerbabuena depression, CCG is the Central Colima Graben and NCG is the North Colima Graben (modified from Norini et al., 2019).

This study integrates data from two distinct acquisitions: the Volcán de Colima Deep Seismic Experiment (CODEX), and the Telemetric Seismic Network of Colima (RESCO) (Figure 2).

RESCO is part of the Centro Universitario de Estudios Vulcanológicos (CUEV) of the University of Colima and is in charge of the seismic monitoring of Volcán de Colima. RESCO has stations distributed over the state of Colima and over the volcano. Here we use data recorded between 2012 and 2017 by 10 stations of the network that consist of broadband Guralp CMG-40TD and CMG-6TD that record in three components at 100 Hz. The CODEX experiment was an IRIS/PASSCAL supported seismic array deployed around Volcán de Colima by the Geophysical Institute at the University of Alaska Fairbanks in collaboration with the Universidad de Colima- Observatorio Vulcanológico (Michael West, 2006). The array consisted of

22 Güralp CMG 40T sensors with Quanterra Q330 digitizers that recorded continuously from 2006 to 2008 in three components at 100 Hz (Figure 2).

Cross-correlation

For all stations, the data is first resampled to 20 Hz and band-pass filtered between 0.01 and 8 Hz. Periods of recordings from the RESCO network that corresponded to eruptions of Volcán de Colima are eliminated. The instrument response for all stations is then removed, along with the mean and the trend.

Earthquakes and local high amplitude spikes that could contaminate the ambient noise wave-field are mitigated by implementing a temporal normalization at 3 times the standard deviation of the daily trace and a spectral whitening between 0.05 and 5 Hz. Station pairs with synchronous recordings are then cross-correlated using MSNoise (Lecocq et al., 2014) for the vertical-vertical (ZZ), and rotated transverse-transverse (TT), and radial-radial (RR). The resulting cross-correlation functions (CCFs) for each pair of stations are then stacked using a phase weighted stacking (PWS), and their symmetric parts are retrieved by averaging their positive and negative lag times.

The PWS has the advantage of enabling the detection of weak but coherent arrivals by exploiting the phase coherence in individual causal and a-causal correlograms and therefore significantly improves the signal to noise ratio in the stacks (Schimmel, 1999; Schimmel and Gallart, 2007; Schimmel and Paulssen, 1997). The whole process resulted in 311 CCFs for each component, respectively.

3.2 Dispersion measurement

The group velocity dispersion curves are estimated using a frequency-time analysis (FTAN) from 0.5 to 10 s (Levshin et al., 1972; Ritzwoller and Levshin, 1998). To prevent the wrong automatic picking of the dispersion curve caused by high-amplitude surface wave overtones or scattered waves, we use a Graphical Users Interface that involves analyst validation (Mordret et al., 2014a). Group velocities from inter-station distances smaller than 1.5 wavelengths and $SNR < 5$ are not considered. The analysis is limited to reasonably covered period ranges with at least 50 measurements, which includes periods between 0.5 and 10 seconds for Rayleigh waves and 0.8 to 8.4 seconds for Love waves.

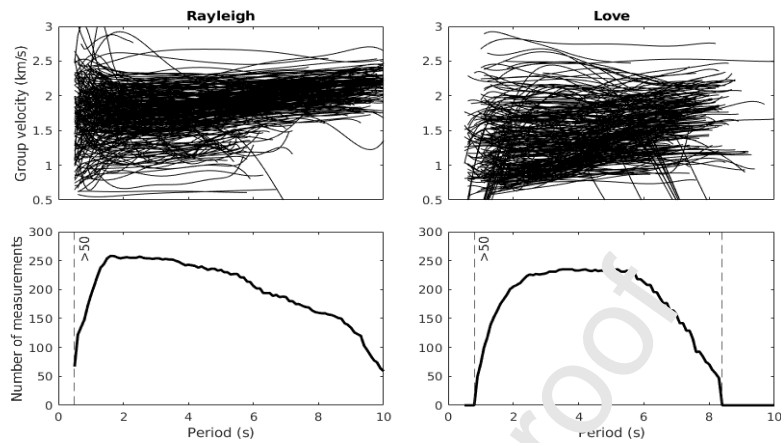


Figure 3. Group velocity measurements for Rayleigh (a) and Love waves (b) obtained using a FTAN analysis. Number of group-velocity measurements as a function of period for Rayleigh (c) and Love waves (d). We restrict our analysis to periods with at least 50 measurements (dashed vertical line).

3.3 Rayleigh and Love Wave Group Velocity Maps

The tomographic inversion of the group-velocity measurements is performed using the Cartesian version of algorithms described by Barmin et al. (2001) and implemented by Mordret et al. (2013). The algorithms are based on ray theory and involve a regularization function composed of a spatial Gaussian smoothing function along with a constraint on the amplitude of the perturbation based on local path density. We use a grid composed of $54 \times 53 = 2862$ square cells with a grid size of 1 km.

The inversion is performed in two steps, with an initial model that has a constant velocity taken as the mean group velocity for each period (Mordret et al., 2014a; Moschetti et al., 2007). The first inversion produces a very smooth map used to identify and reject measurements with travel time residuals greater than two standard deviations. The remaining measurements are used in the second inversion to produce the final group velocity maps. The procedure does not account for the topography. The error of the flat topography approximation on the velocity was estimated by Brenguier et al. (2007) and Mordret et al. (2014b) to be less than 5%. Such an error should therefore be negligible compared to the group velocity variations of over 30% at each period.

The group velocity measurements and coverage along with the path density for the respective periods are shown for Rayleigh and Love waves in Figure 4 and 5 (d-f and g-i), respectively. Both Volcán de Colima and the Nevado de Colima are covered by a dense coverage of at least 8 ray paths for all 3 periods. The group-velocity maps for Rayleigh and Love waves, where lateral velocity variations can be observed at periods of 2, 4 and 6 s, are shown in Figure 4 and 5 (a-c), respectively. The locations shown and interpreted have at least four rays per cell. A variance reduction of the travel-time residuals exhibits values ranging from 72 to 79% and 88 to 93% for Rayleigh and Love waves respectively, indicating that the retrieved velocity maps fit the data well. The mean velocity of the maps increases slightly with the period for both Rayleigh and Love waves, going from 1.79 to 1.94 km/s and 1.29 to 1.63 km/s respectively, in good agreement with the dispersion curves shown in Figure 3. At all periods, we observe an elongated low velocity zone that extends from the center of Volcán de Colima to the SW direction (Figure 4 and 5 a-c). The Love wave group velocity maps display a similar global velocity structure pattern as for Rayleigh waves, with the exception of small low velocity zones.

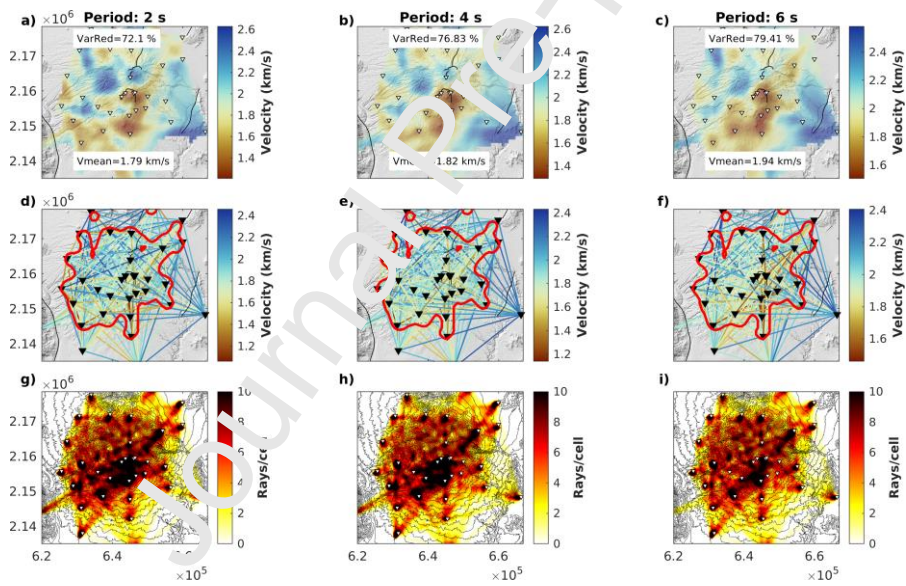


Figure 4. Rayleigh group velocity maps at 2, 4 and 6 seconds (a-c respectively). Rayleigh-wave group velocities associated with each path at 2, 4 and 6 seconds (d-f). The red contours show the limit of the study area with 4 paths per cell. Ray-path densities per cell at 2, 4 and 6 seconds (g-i).

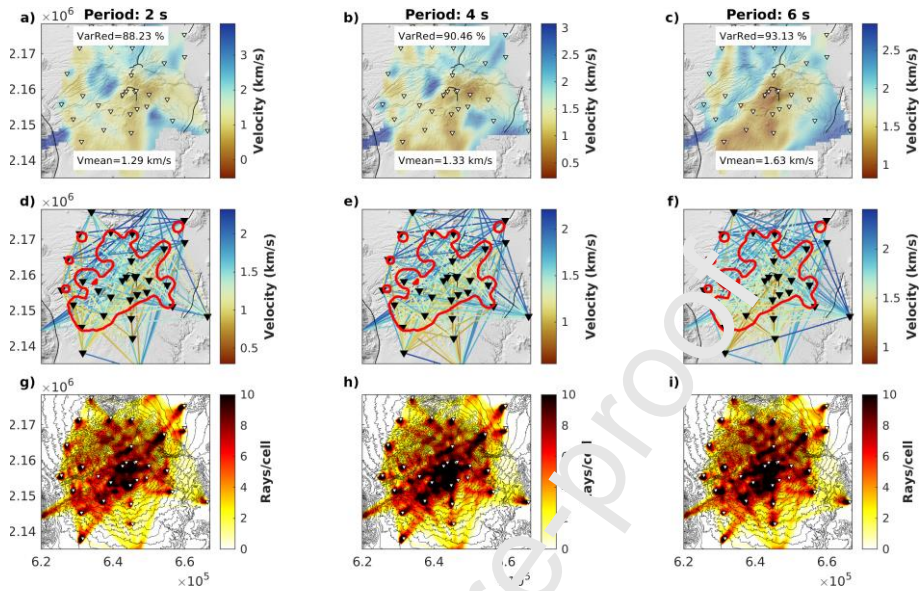


Figure 5. Love-wave group velocity maps at 2, 4 and 6 seconds (a-c respectively). Love-wave group velocities associated with each path at 2, 4 and 6 seconds (d-f). The red contours show the limit of the study area with 4 paths per cell. Ray-path densities per cell at 2, 4 and 6 seconds (g-i).

The accuracy of the size and location of the retrieved anomalies is assessed through the evaluation of the resolution matrix associated with each inversion (Barmin et al., 2001; Mordret et al., 2015, 2013). For each cell of the model, the corresponding line of the resolution matrix represents the response of the tomographic process to a Delta function type anomaly with the size, the shape, and the location of the output spot indicating how accurately the anomaly can be retrieved. The precision of the location of the recovered spike varies slightly depending on the station coverage.

The entire resolution matrix at 2, 4, and 6 s for Rayleigh and Love waves are shown in Figure 6 and Figure 7, respectively. Here, with a grid cell size of 1 km, a resolution shift <0.5 km means that the center of the retrieved anomaly is in the same cell as the input spike.

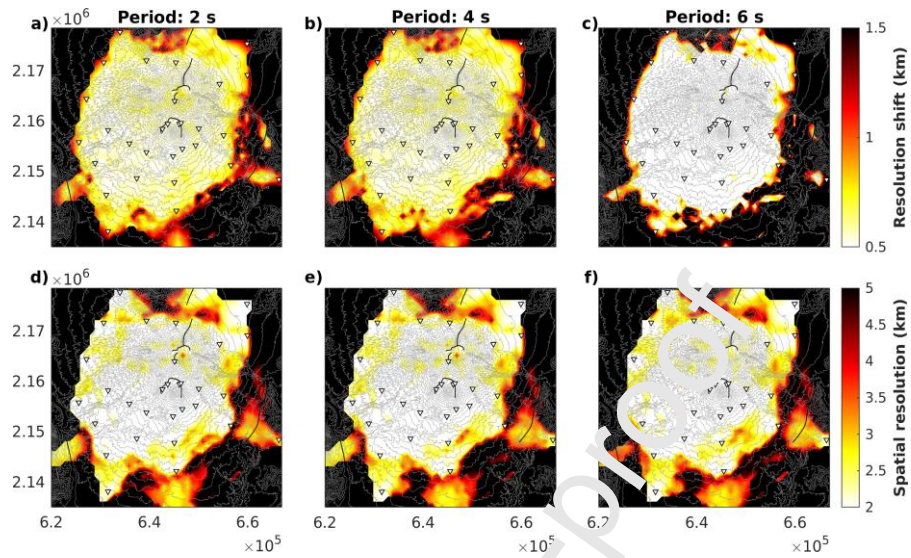


Figure 6. Resolution shift for Rayleigh waves at 2,4 and 6s (a-c). A resolution shift <0.5 km indicates that the center of the retrieved anomaly is in the same cell as the input spike. Spatial resolution maps (d-f).

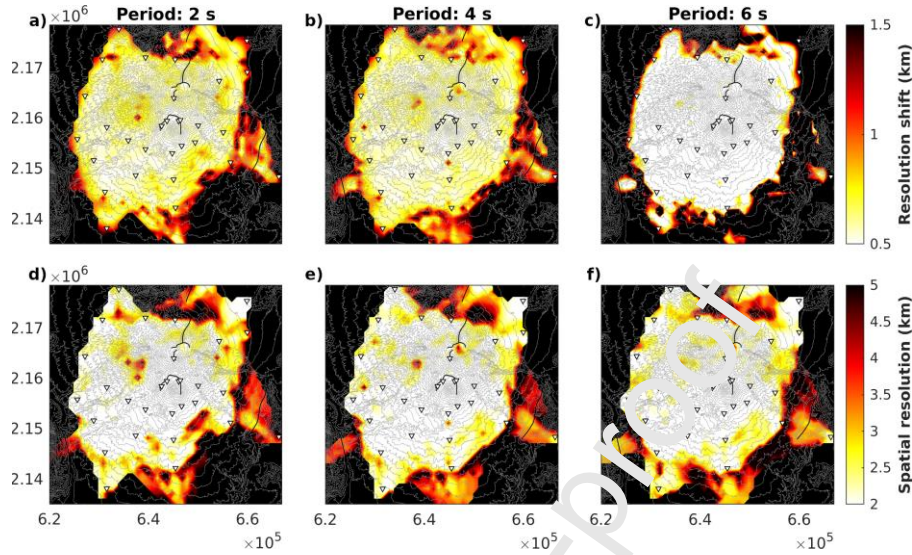


Figure 7. Resolution shift for Love waves at 2, 4 and 6s (a-c). A resolution shift <0.5 km indicates that the center of the retrieved anomaly is in the same cell as the input spike. Spatial resolution maps (d-f).

3.4 Depth inversion

Rayleigh and Love waves group velocity maps are like a gather of local group velocity dispersion curves with group velocity measurements at different periods for every particular location on the map.

A 1-D local layered velocity model can then be assessed by inverting these local dispersion curves for each cell of the grid. For this inversion we use a Monte-Carlo global direct-search technique, the Neighborhood Algorithm developed by Sambridge (1999) and described in detail in Mordret et al. (2013). The solution space is sequentially and non-uniformly sampled while considering the data fit from old samples.

The parametrization here is similar to Mordret et al. (2014b) and uses a power law backbone velocity profile to take into account the possible slow velocities in the shallow layers due to weathering and alteration overlaid with smoothly varying velocity anomalies and anisotropy. Along with two parameters controlling the power law backbone velocity profile (the surface velocity and the curvature of the velocity profile, respectively) we use five cubic B splines that parametrize the overlaid velocity anomalies. To reduce the number of parameters to be inverted, these continuous functions are discretized into 33 layers. For each layer, we consider a constant shear-wave velocity (V_s) and the parameter ranges allowed are generally

defined based on the plausible crustal models in a volcanic region, allowing a large variability to resolve both low and high velocity body.

For the initial isotropic inversion, a total 25,000 V_{sv} and V_{sh} are sampled for each cell of the grid, and the best-fitting 300 models are kept to calculate a mean model resulting in a 3D V_s model of the volcano. The anisotropic and isotropic models are compared to evaluate the necessity of an anisotropic inversion. The anisotropic inversion was parametrized using an additional four dedicated cubic B splines for a complete parametrization of 13 parameters. In this case, a total 19,000 models are samples for each cell of the grid.

The V_s isotropic model or effective S wave velocity at each location is computed from V_{sh} and V_{sv} via a Voigt's average which better reflects the isotropic variations in elastic properties (Dziewonski and Anderson, 1981; Ekström and Dziewonski, 1998):

$$V_s = \sqrt{\frac{2V_{sv}^2 + V_{sh}^2}{3}}$$

The average model is removed from the resulting 3D V_s model to obtain the 3D V_s anomaly model presented and interpreted below. The difference between V_{sv} and V_{sh} , called radial anisotropy (ξ), is represented as the percentage difference between V_{sh} and V_{sv} in the medium (Jaxybatatou et al., 2014; Mordret et al., 2014b):

$$\xi = \frac{V_{sh} - V_{sv}}{V_s}$$

Figure 8 shows the best fit to isotropic and anisotropic dispersion curves at two different locations. On average over the whole studied area, anisotropic parameterization reduces the misfit by $\sim 40\%$. The isotropic inversion has particularly poor results below ~ 5 s period, after which a better fit can be observed between the measured and the synthetic dispersion curves. This indicated the need for an anisotropic inversion with the additional parametrization focused on the upper 5 km depth. This could indicate that the radial anisotropy is limited to shallow depths, although this is probably caused by a lack of dispersion measurements for Love waves at longer periods combined with a shallower depth sensitivity compared to Rayleigh wave at corresponding periods (Figure 9).

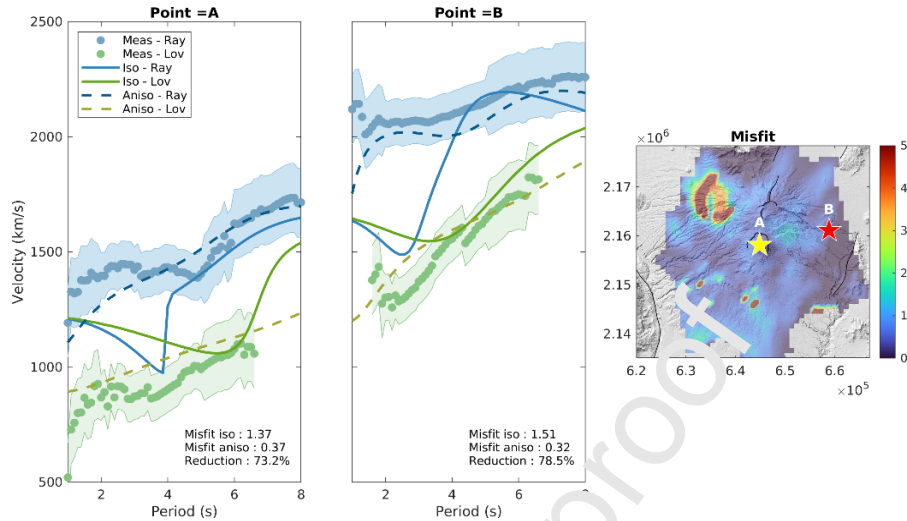


Figure 8. Best synthetic Rayleigh and Love group velocity dispersion curves at points A and B for an isotropic and anisotropic inversion. The blue and green curves are the best fitting isotropic dispersion curves for Rayleigh and Love waves, respectively. The blue and green dashed-curves are the best fitting anisotropic dispersion curves for Rayleigh and Love waves, respectively. The blue and green dots with the blue and green areas are the measured Rayleigh and Love wave dispersion curves, respectively, with their uncertainties. The map shows the misfit of the final model and the location of points A and B (yellow and red markers, respectively).

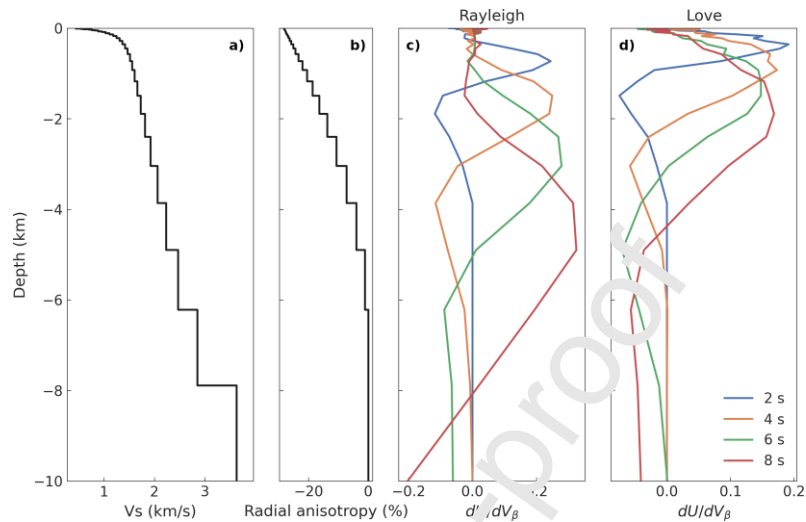


Figure 9. V_s velocity (a) and radial anisotropy (b) profile at point A, and the corresponding sensitivity kernel at 2, 4, 6, and 8 s for the fundamental mode Rayleigh (c) and Love (d) wave group velocity. The sensitivity kernels were calculated using the open source software developed by Herrmann (2013). The maximum sensitivity depth is much shallower for Love waves than for Rayleigh waves, limiting the analysis of the radial anisotropy above 5 km depth.

Each cell of each model is eventually shifted according to the altitude of the considered point to show values at depths relative to the sea level. The uncertainty and the misfits of the final 3D V_s model are shown in Figure 10 and Figure 8, respectively. Parts of the model deeper than ~ 3 km b.s.l. are less constrained, with larger uncertainties likely caused by the lack of long period measurements. From the final 3D V_s model, V_s anomaly and the radial anisotropy, we extracted horizontal slices at 1 km a.s.l., sea level, and 4 km b.s.l. (Figure 11) along with vertical slices (Figure 12).

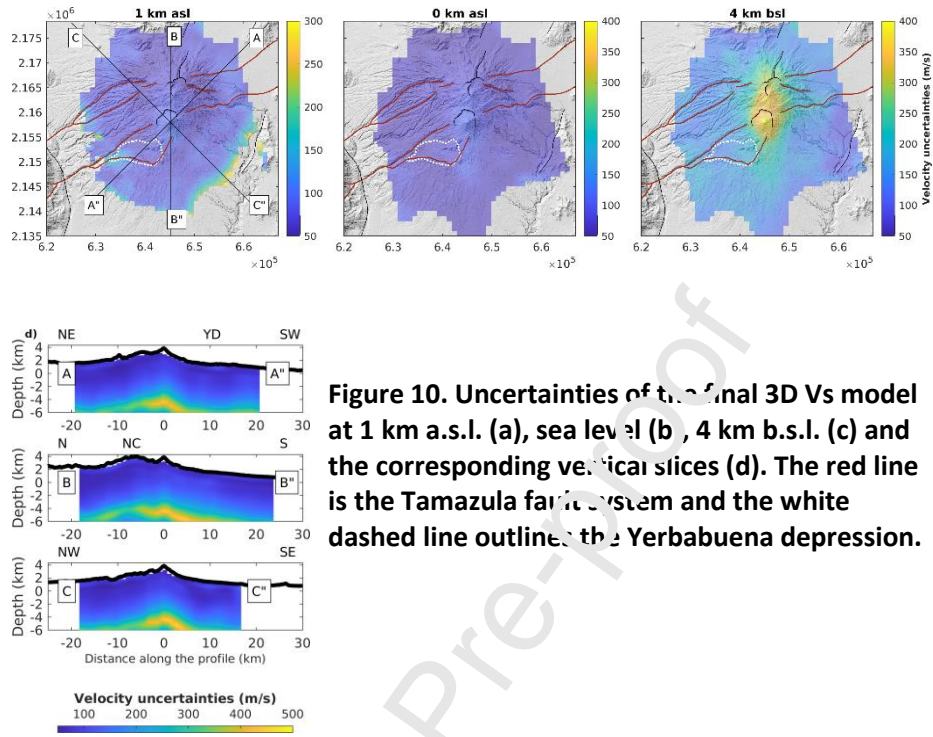


Figure 10. Uncertainties of the final 3D Vs model at 1 km a.s.l. (a), sea level (b), 4 km b.s.l. (c) and the corresponding vertical slices (d). The red line is the Tamazula fault system and the white dashed line outlines the Yerbabuena depression.

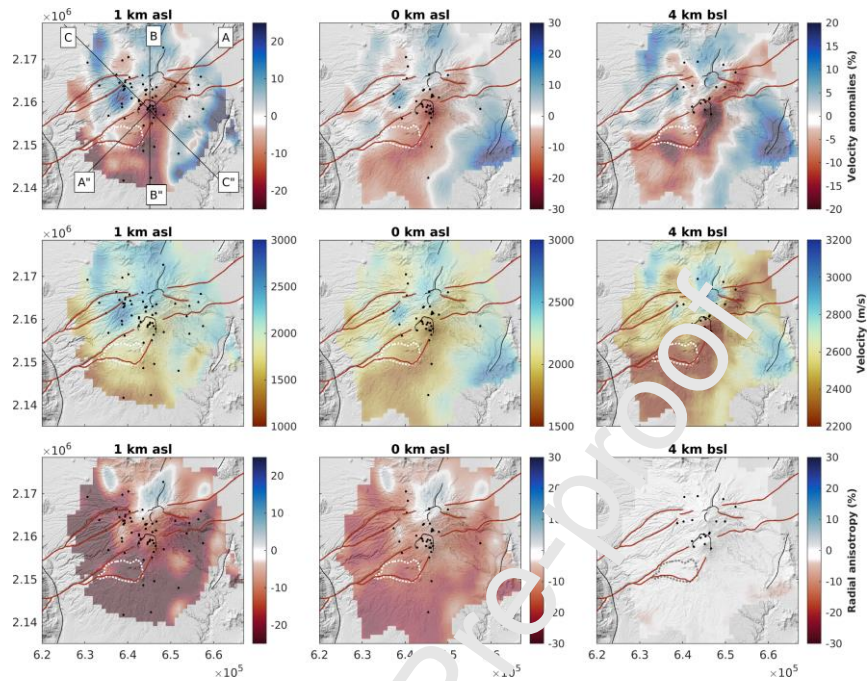


Figure 11. Horizontal slices through the V_s anomaly model at 1 km above sea level, and 4 km below sea level (a-c). The absolute velocities of the isotropic V_s model for the corresponding depth (d-f). Below, Same as above but for the radial anisotropy (g-i). The red line is the Tamazula fault system and the white dashed line outlines the Yerbabuena depression. The black dots indicate the projection of the hypocenters within 1km of the slice depth of volcano tectonic events from 2019-2021 calculated using the velocity model of Núñez-Cornú et al. (1994).

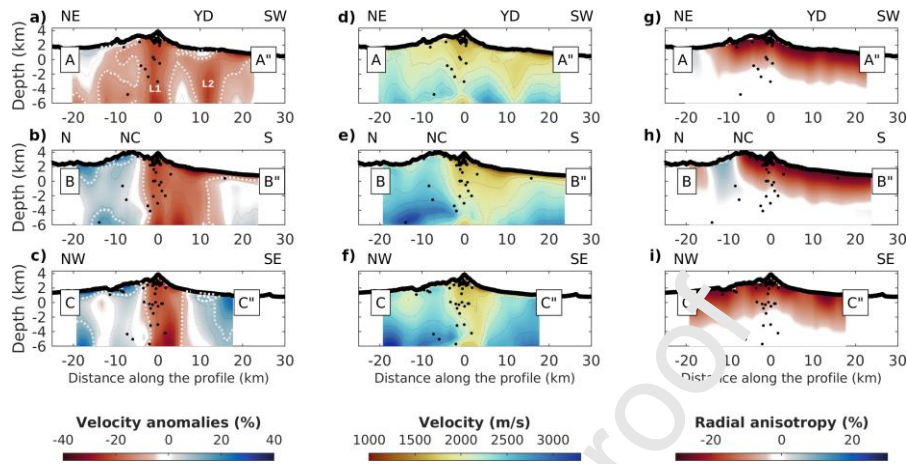


Figure 12. Vertical slices through the Vs anomaly model (a-c), the Vs velocity model (d-f), and the radial anisotropy (g-i). The location and orientation of the slices are shown in Figure 11a. The distance along the profile is calculated from the crater of Volcán de Colima. The white dashed lines highlight the -10 and +10% contours. The location of the Nevado de Colima along profile B-B'' is identified as NC and D identifies the location of the Yerba-buena depression along profile A-A''. The black dots indicate the projection of the hypocenters within 500 m of the profile of volcano tectonic events from 2019-2021 calculated using the velocity model of Núñez-Cornú et al. (1994).

4. Interpretation and Discussion

We built a high-resolution shear-wave velocity model of Volcán de Colima down to 6 km b.s.l. The model includes the Nevado de Colima, Volcán de Colima and a good portion of its southern flank. The Cántaro is the only part of the CVC that is notable missing from our observations. Nevertheless, this study includes most structures of the CVC observed in other geophysical and geological studies, with a finer resolution than past ambient seismic noise tomographies.

4.1 Shear wave velocity and anomaly

The group velocity maps show a consistent low velocity zone trending from NE to SW with very little lateral variation from 2s to 6s (Figures 4 and 5 a-c). This anomaly has been similarly observed by the local-scale ambient noise tomography by Escudero and Bandy (2017), who also used CODEX data to retrieve Rayleigh wave velocity maps of the CVC at 3 and 5s. Notably, their mean velocity of 1.8 km/s for Rayleigh waves is relatively close to the ones observed in this study ranging from 1.79 to 1.94 between 2 and 6 s.

The ambient seismic noise based regional V_s model by Spice et al. (2017) displays a similar low velocity anomaly at 4 km depth under Volcán de Colima. In their case, the anomaly appears much larger, which they acknowledge as a possible consequence of the low horizontal resolution of their regional tomography and that, in turn, could cause spatial smearing when trying to image a body of this size. The low velocity in our 3D V_s model has a distinct NE-SW orientation and is limited at its northern border by the Nevado de Colima (Figure 11). A major portion of the Nevado de Colima is associated with a high-velocity anomaly that extends to the north and at depth.

High velocity zones on volcanoes are not uncommon and are typically associated with solidified dikes or sills that formed during past eruption history of the volcano. The Piton de la Fournaise volcano has such magma path intrusions at depth that were revealed as high velocity anomaly by ambient noise tomography (Mordret et al., 2014b), gravimetry (Gailler et al., 2009), and drilling (Lerebour et al., 1989). Similar high velocity anomalies have been revealed by local earthquake tomography beneath the Popocatepetl (Kuznetsov and Kozlov, 2014) and the Asama Volcano (Aoki et al., 2009).

The southward orientation of the low-velocity anomaly is roughly consistent with the north-south trend of the chain of three andesitic stratovolcanoes that compose the quaternary CVC. This configuration has caused speculations about a gradual trenchward shift of the magmatic front of the CVC in the frame of a long-lasting southward migration of the magma pathways dating from the formation of the Cántaro Volcano (e.g., Alvarez and Yutsis, 2015; Luhr and Carmichael, 1980).

The CVC had at least 12 gravitational collapses during the past 45,000 years, nine of which occurred at volcán de Colima during the past 22,000 years (Borselli et al., 2011). Roverato et al. (2011) attribute such a collapse rate to the continuous magmatic recharge in the volcanic system, the regional and the local stress regime by the Colima Graben, and the Tamazula Fault whose extensional NW–SE vector has promoted sector collapses of the CVC to the SW. The location of the low-velocity anomaly to the south of the Nevado de Colima is consistent with the multiple sector collapses of both Nevado de Colima and Paleofuego volcanoes, although it is too deep to be explained by this element alone (e.g., Sychev et al., 2019). Such collapses generate stress perturbations due to unloading caused by mass redistribution. At some volcanoes, the lateral flank failures were followed by a modification of the shallow plumbing system (Maccaferri et al. 2017). The low-velocity anomaly could contain a magma reservoir that cannot be easily distinguished from shallow volcanic deposits

and soft fluid saturated rocks. The volcano tectonic hypocenters likely provide evidence that the low velocity zone below Volcán de Colima hosts the magmatic plumbing system feeding the volcano. The location of the hypothetical shallow magma reservoir to the south of the main vent has led to speculations that the parasitic domes of Los Hijos, on the southern flanks of Volcán de Colima, feeds from the same source, further indicating a southward migration of the volcanism of the CVC (Alvarez and Yutsis, 2015; Sychev et al., 2019).

The presence of Los Hijos, along with the Volcancito parasitic cone on the north-eastern flank of Volcán de Colima, led Garduño-Monroy et al. (1998) to associate the aforementioned potential migration of volcanism with the NE-SW Tamazula Fault (TF) system. This system, mostly composed of normal faults, is believed to have weakened the crust and serve as a path for magma migration and, along with the associated stress field, is responsible for the flank instability of the CVC (Cortés et al., 2010; Garduño-Monroy et al., 1998). In contrast, some of the features attributed to the TF have been also interpreted as the result of active gravitational spreading of the volcanic complex by Norini et al. (2019, 2010). With the NE-SW orientation of the low velocity anomaly in our 3D Vs model parallel to the TF system (Figure 11) we can speculate that this is more in agreement with a regional whole-crustal structure that facilitates magma migration beneath CVC.

Sychev et al. (2019) built 3D models of the P and S wave velocities and attenuation for the CVC from the body waves of local earthquakes recorded by CODEX. They observed the same distinction between a high velocity zone under the Nevado de Colima and a low velocity anomaly to the south of Volcán de Colima. By extrapolating it at depth as a south dipping structure that reaches the lower crust, they interpret the TF as a mechanically weakened zone that forms a pathway to feed CVC after a transition at ~15 km depth.

The alignment of our low velocity zone along the TF does not unequivocally prove that the fault system is the deeply rooted structure guiding magma to the surface. We therefore cannot exclude the interpretation by Norini et al. (2019, 2010) that the fault system has been originated by gravitational spreading rather than by regional active tectonics. Nevertheless, there is increasing geophysical evidence showing a relationship between the TF and a regional whole-crustal structure that contributes to magma migration towards the surface.

The shallow extensional activity of the segment of TF within the Colima Graben could be the result of a deeper regional active tectonics combined with topographic configuration of the volcanic complex, the weakness of the underlying sedimentary graben fill, and of the geometry of the regional basement. Such a concept would also help explain the lack of seismicity specifically associated with this segment of the fault system, as opposed to the crustal earthquakes observed in its Manzanillo section.

Unlike Sychev et al. (2019), our model does not reach 15 km depth. However, the low velocity anomaly appears as a consolidated structure down to 6 km b.s.l. that is ~15 km wide in the B-B'' profile and ~10 in the C-C'' profile. The A-A'' profile, however, displays two distinct vertical structures that connect at ~2 km b.s.l (L1 and L2, Figure 12a). Previous estimates place a shallow magma chamber at 6.3 km below

the summit based on the depth of the hornblende stability region for the 1998–1999 erupted lavas (Luhr, 2002) and the top at about 1.5 km depth below sea level based on a low-density body in the gravimetric model of Medina et al. (1996).

The observation of an aseismic zone between 4 and 7 km depth during the 1991 and 1997–2000 activity of the volcano is believed to further indicate the existence of this shallow magma reservoir below the summit (Núñez-Cornú et al., 1994; Zobin et al., 2002). All those estimates place a shallow magma chamber at a depth where our model provides reliable observation of a low velocity anomaly.

4.2 Radial anisotropy

The combination of the shallower maximum sensitivity depth of Love waves compared to Rayleigh waves and the lack of long period measurements for Love wave dispersion curves caused the radial anisotropy to be apparently limited to above 5 km depth in our results.

Nevertheless, the association of a fault system with the magma transport under the CVC is supported by the radial anisotropy results. We focus this part on the interpretation on the sign of the radial anisotropy because the simplifications in the inversion procedure, ignoring the topography and the P wave anisotropy, likely have biased its absolute value. In a similar context, however, Xie et al. (2013) and Mordret et al. (2014b) showed that the sign should be robust.

In a volcanic environment and at crustal depths, radial anisotropy can be a very good indicator of the dominant fabric within the magmatic system and, consequently, of the dominant type of intrusion. Partial melting can produce radial anisotropy with oriented volcanic fluid-filled cracks strongly affecting the macro-mechanical properties of the material (e.g., Gudmundsson, 2011), with common interpretations pointing towards the presence of sill layering, lava flows, dike networks or lenses of partial melt. For example, sill layering tends to produce positive radial anisotropy because V_{sv} is globally slowed down due to the presence of molten material piled horizontally (Jaxybulatov et al., 2014). Alternatively, active dike networks would yield a negative anisotropy because their vertically oriented structure would slow down V_{sh} (e.g., Lopez et al., 2021; Mordret et al., 2014b).

A negative radial anisotropy dominates the edifice above 5 km depth indicating dominant vertical structures such as steep normal faults, jointing, and magmatic dike intrusions. Some of these structures are exposed at the surface, such as the three subvertical N-S-trending dikes crop out identified by Norini et al. (2010) in the inner wall of the Paleofuego collapse scar. The N-S orientation of these dikes parallels the alignment of the Nevado de Colima, Volcán de Colima, and Los Hijos domes and are interpreted as evidence that the magma storage of the active CVC is drained by a network of N-S-trending dikes.

Magmatic fluids are typically expected to accumulate in shallow magma-chambers in horizontally extensive, overlapping sill-like structures (e.g., Jaxybulatov et al., 2014)

or horizontal lenses (Fournier, 1999). Nevertheless, the alignment of the low velocity anomaly in our model with the TF suggests a development of magma ascent along fault lines and shear zones that is further confirmed by the negative radial anisotropy. This association indicates that faults and vertical magma-filled dikes are the likely dominant structure in the edifice. Furthermore, the negative radial anisotropy identified by Spica et al. (2017) under the CVC seems to extend deeper through the crust, giving additional evidence of vertically extensive fluid-filled fractures in the crust.

A preexisting fault zone such as the CR included potentially deep reaching structures. This provides a natural pathway for fluids, with the high-permeability damage zone and the low-permeability fault core, to allow magma to ascent to the surface (e.g., Shelly et al., 2013).

Another interesting feature comes from the concurrent modeling of the gravimetric and magnetic anomalies by Alvarez and Yutis (2015). They identified two low density/ high magnetic susceptibility anomalies, interpreted as magma bodies, up to ~1.5 km b.s.l. that correspond with the first and the second negative anomaly along the A-A'' profile of our model (L1 and L2 respectively, Figure 12a). Between them they identify a higher density anomaly at a depth of ~1.2 km b.s.l. below the Yerbabuena depression that corresponds with the middle vertical anomaly along the A-A'' profile of our model. They interpret this structure as a now solidified intrusion that induced a local gravity collapse following its cooling. These features are additional evidence pointing towards a southward migration of the volcanism in the CVC, although they don't provide clear insights on the mechanism behind that change. Alvarez and Yutis (2015) identified another low-density region south of the Yerbabuena depression that they called the "Southern Magma Body" and interpreted as molten material. Although our results cannot confirm the presence of magma in that area of the model, that low density body corresponds to the southernmost vertical low velocity anomaly along the A-A'' profile (L2, Figure 12a) and should be further investigated.

In the absence of supporting evidence for a magma reservoir at such shallow depths, the hydrothermal alteration could offer an alternative explanation for the observed velocity anomaly. Low-velocity anomalies in the shallow crust have been found on other volcanoes such as Uturuncu volcano in the Andes (Jay et al., 2012), and Mount St. Helens (Wang et al., 2017) where they interpreted the low-velocity anomaly as a highly fractured volume containing the magma conduit and hydrothermal systems, but with most of the pore space in the volume likely filled with hydrothermal fluids rather than melt.

Heap et al. (2021) looked at laboratory data for altered rhyodacites from Chaos Crags (Lassen volcanic center) to ultimately emphasize that both the porosity-decreasing alteration they explored and porosity-increasing alteration can promote volcano instability and collapse, although by different mechanisms. This, in turn, could increase the likelihood of volcano spreading, flank collapses, and phreatic/phreatomagmatic explosions. This could be linked with the elevated collapse rate of the CVC with the progressive weakening of the volcanic edifice by hydrothermal alteration as a main indirect endogenous factor (Roverato et al., 2011).

The location of the low velocity zones relative to the TF establishes a strong apparent relationship between the fault system and intrusive bodies that use such a natural path of weakness to ascend through networks of interfingered dikes. Basement fault activity beneath the volcanic edifice could have contributed to both the formation of the TF and the frequent flank collapses at the CVC (e.g., Vidal and Merle, 2000). A more comprehensive study of the seismicity using the decades of existing seismic data would help to better investigate the tectonic structure in the CVC and how they relate to active magma pathways in the crust.

Because the radial anisotropy alone does not fully support a fault-assisted magma migration, further attention should be paid to possible processes behind it. Theoretical and field studies have overwhelmingly indicated that magma pathways are determined by host rock stresses, with magma moving along the path of minimum energy within a volcanic edifice (e.g., Rivalta et al., 2019). Magma ascends to the surface through dikes that align themselves with the most energy-efficient orientation, roughly perpendicular to the least compressive principal stress axis σ_3 .

Along with structural features, stress is attributed to generating the anisotropy observed in the crust (e.g., Johnson et al., 2011). In turn, both the local stress field and inherent structures (topography, fault, collapsed caldera structure, etc.) also impact the development of complex magma plumbing systems (Caussard and Amelung, 2014; Tibaldi, 2015). This allows for distinguishing between regions of stress-induced and structural anisotropy around volcanoes (e.g., Johnson et al., 2011).

A better understanding of the stress conditions in the crust of the CVC could help put in perspective their impact on volcanic structures and processes, the observed anisotropy, and potentially the TF. Massaro et al (2020) analyzed the stress-filled of the CVC by integrating published geophysical, volcanological, and petrological data into a 2D finite-element model. Their modeling indicates that the majority of stress variations are located at the top of the magma chambers, implying a close-to-equilibrium state of the volcano associated with a stress distribution induced by a feeding system directly connected to the surface. This is in agreement with the long-lasting open conduit dynamics that have lasted since 1913. Nevertheless, the low-velocity anomaly could come in part from the contribution of a highly fractured region beneath the volcanic edifice generated by stress reorganization above the magma storage, providing magma pathways to the surface (e.g., Wang et al., 2017).

When it comes to the negative radial anisotropy, Spica et al. (2017) emphasized that the shear strain in extensional contexts preferentially orient the seismic slow axes of the minerals along the vertical axis which is expected to induce a positive radial anisotropy (e.g., Mainprice et al., 2000). The negative radial anisotropy is, therefore, evidence that the shape-preferred orientation of vertical structures in the crust, likely guiding fluids toward the surface, dominates over the crystallographic preferred orientation at the CVC.

4.3 Insights from petrology

Petrological and geochemical studies focused on the CVC suggest the existence of a complex underlying magmatic plumbing system, involving multiple magma storage

levels from the base of the crust to a shallow-level upper crustal magma storage region, with deposits such as those of the major 1913 Plinian eruption of volcán de Colima revealing a particular process of magma mixing or mingling (Crummy et al., 2014). Pressure estimates from two-pyroxene barometry by Hughes et al. (2021) suggest a magma mixing, crystallization, and remobilization at 15 km depth, in the deep mushy magma storage identified by other seismic tomographies (Spica et al., 2017; Sychev et al., 2019), prior to migration to a ‘spongy’ shallow magma reservoir.

Studies based on melt inclusions consistently show melt inclusion entrapment depths in vapor saturated conditions of typically <8 km for interplinian activity (Atlas et al., 2006; Reubi et al., 2013; Reubi and Blundy, 2008). While the melt inclusions from the major 1913 Plinian eruption reveal depths of entrapment ranging from 8.8 to 11.1 km, depths recorded by the 1998–2005 melt inclusions indicate that the magma from those recent eruptions was shallowly stored (Reubi et al., 2013). This likely matched the seismically active low-velocity anomaly identified in our results. Atlas et al. (2006) also analyzed melt inclusions of Volcán de Colima that they determined were trapped at depths of >12 km, and suggest that vapor-saturated crystallization most likely occurred during the ascent in a series of interconnected conduits in which mixing is allowed rather than a large stratified magma chamber. This corresponds to the overwhelming negative radial anisotropy we observed pointing toward vertically oriented structures, such as dikes and cracks as the source of the negative anomaly.

5. Conclusion

We used the group dispersion curves of Rayleigh and Love waves extracted from ambient seismic noise recorded on Volcán de Colima Complex to build a high-resolution 3D model of the shear wave velocity and the radial anisotropy in the upper-crust.

The results indicate a network of deeply rooted NE-SW oriented low velocity zones, parallel to the Tomazula fault, that connect at ~2 km b.s.l. This structure overlaps a region of negative radial anisotropy that indicates that magma under volcán de Colima follows vertically oriented structures. In contrast, a distinct high-velocity anomaly under Nevado de Colima highlights the distinction between the former active system, filled with solidified dikes and sills, and the current one, associated with a network of fluid-filled dikes.

This also indicates that the current shallow magma storage is dominated by vertically oriented intrusion, rather than a large single volume of melt. As other seismic tomographies (e.g., Escudero and Bandy, 2017; Spica et al., 2017; Sychev et al., 2019), we speculate that the regional tectonics, specifically the Colima Rift combined with a deeply rooted fault system, play a critical role in the transport of magma from a deeper system through the weakened crust of the volcanic complex. Our results offer the clearest insight to date on the internal structure of Volcán de Colima, including the southward migration of the intrusions. This evolution is already evidenced at the surface with structures Los Hijos parasitic domes and the

Yerbabuena depression which serve as indications of the further development of the Colima Volcanic Complex.

Acknowledgements

This research was supported by the CONACYT-299766 and CONACYT CF 2019 – 58547 grants and Raphael S. M. De Plaen acknowledges support from a UNAM-DGAPA postdoctoral scholarship. D. M. Vargas-Bracamontes is grateful to CONACYT's project PDCAPN 2579. We thank Luca De Siena and an anonymous reviewer for their in-depth review and comments that helped improve the manuscript.

Data Availability

CODEX data are available through IRIS network ZA, doi: 10.7914/SN/ZA_2006) and the RESCO data are available through the University of Colima. The Velocity model has been deposited at Zenodo (10.5281/zenodo.6475834).

References

- Allan, J.F., 1986. Geology of the Northern Colima and Zacoalco Grabens, southwest Mexico. Late Cenozoic rifting in the Mexican volcanic belt. *Geol. Soc. Am. Bull.* 97, 473–485. [https://doi.org/10.1130/0016-7606\(1986\)97<473:GOTNCA>2.0.CO;2](https://doi.org/10.1130/0016-7606(1986)97<473:GOTNCA>2.0.CO;2)
- Alvarez, R., Yutsis, V., 2015. Southward Migration of Magmatic Activity in the Colima Volcanic Complex, Mexico: An Ongoing Process. *Int. J. Geosci.* 06, 1077–1099. <https://doi.org/10.4236/ijg.2015.69085>
- Aoki, Y., Takeno, M., Aoyama, H., Fujimatsu, J., Matsumoto, S., Miyamachi, H., Nakamichi, H., Ohkura, T., Ohminato, T., Oikawa, J., Tanada, R., Tsutsui, T., Yamamoto, K., Yamamoto, M., Yamasato, H., Yamawaki, T., 2009. P-wave velocity structure beneath Asama Volcano, Japan, inferred from active source seismic experiment. *J. Volcanol. Geotherm. Res.* 187, 272–277. <https://doi.org/10.1016/j.jvolgeores.2009.09.004>
- Atlas, Z.D., Dixon, J.E., Sen, G., Finny, M., Martin-Del Pozzo, A.L., 2006. Melt inclusions from Volcán Popocatepetl and Volcán de Colima, Mexico: Melt evolution due to vapor-saturated crystallization during ascent. *J. Volcanol. Geotherm. Res.* 153, 221–240.

- <https://doi.org/10.1016/j.jvolgeores.2005.06.010>
- Barmin, M.P., Ritzwoller, M.H., Levshin, A.L., 2001. A fast and reliable method for surface wave tomography. *Pure Appl. Geophys.* 158, 1351–1375.
- Borselli, L., Capra, L., Sarocchi, D., De la Cruz-Reyna, S., 2011. Flank collapse scenarios at Volcán de Colima, Mexico: A relative instability analysis. *J. Volcanol. Geotherm. Res.* 208, 51–65.
<https://doi.org/10.1016/j.jvolgeores.2011.08.004>
- Brenguier, F., Shapiro, N.M., Campillo, M., Nercessian, A., Ferrazzini, V., 2007. 3-D surface wave tomography of the Piton de la Fournaise volcano using seismic noise correlations. *Geophys. Res. Lett.* 34, 2–6.
<https://doi.org/10.1029/2006GL028586>
- Capra, L., Gavilanes-Ruiz, J.C., Bonasia, R., Saucedo Girón, R., Sulpizio, R., 2015. Re-assessing volcanic hazard zonation of Volcán de Colima, México. *Nat. Hazards* 76, 41–61. <https://doi.org/10.1007/s11069-014-1480-1>
- Castellanos, J.C., Clayton, R.W., Pérez-Camacho, X., 2018. Imaging the Eastern Trans-Mexican Volcanic Belt With Ambient Seismic Noise: Evidence for a Slab Tear. *J. Geophys. Res. Solid Earth* 123, 7741–7759.
<https://doi.org/10.1029/2018JB015783>
- Cortés, A., Garduño, V.H., Macías, J.L., Navarro-Ochoa, C., Komorowski, J.C., Saucedo, R., Gavilanes, J.C., 2010. Geologic mapping of the Colima volcanic complex (Mexico) and implications for hazard assessment. *Spec. Pap. Geol. Soc. Am.* 464, 249–264.
[https://doi.org/10.1130/SPE510.2464\(12\)](https://doi.org/10.1130/SPE510.2464(12))
- Domínguez, T., Zobin, V.M., Reyes-Davila, G.A., 2001. The fracturing in volcanic edifice before an eruption: The June-July 1998 high-frequency earthquake swarm at Volcán de Colima, México. *J. Volcanol. Geotherm. Res.* 105, 65–75. [https://doi.org/10.1016/S0377-0273\(00\)00243-2](https://doi.org/10.1016/S0377-0273(00)00243-2)
- Dziewonski, A.M., Anderson, D.L., 1981. Preliminary reference Earth model. *Phys. Earth Planet. Inter.* 25, 297–356. [https://doi.org/10.1016/0031-9201\(81\)9046-7](https://doi.org/10.1016/0031-9201(81)9046-7)
- Ekström, G., Dziewonski, A.M., 1998. The unique anisotropy of the Pacific upper mantle. *Nature* 394, 168–172. <https://doi.org/10.1038/28148>
- Escudero, C.R., Bandy, W.L., 2017. Ambient seismic noise tomography of the Colima Volcano Complex. *Bull. Volcanol.* 79.
<https://doi.org/10.1007/s00445-016-1096-2>
- Ferrari, L., 2004. Slab detachment control on mafic volcanic pulse and mantle heterogeneity in central Mexico. *Geology* 32, 77–80.
<https://doi.org/10.1130/G19887.1>
- Ferrari, L., Orozco-Esquivel, T., Manea, V., Manea, M., 2012. The dynamic

- history of the Trans-Mexican Volcanic Belt and the Mexico subduction zone. *Tectonophysics* 522–523, 122–149.
<https://doi.org/10.1016/j.tecto.2011.09.018>
- Ferrari, L., Rosas-Elguera, J., 2000. Late Miocene to Quaternary extension at the northern boundary of the Jalisco block, western Mexico: The Tepic-Zacoalco rift revised. *Spec. Pap. Geol. Soc. Am.* 334, 41–63.
<https://doi.org/10.1130/0-8137-2334-5.41>
- Fournier, R.O., 1999. Hydrothermal processes related to movement of fluid from plastic into brittle rock in the magmatic-epithermal environment. *Econ. Geol.* 94, 1193–1211.
<https://doi.org/10.2113/gsecongeo.94.8.1193>
- Gailler, L.S., Lénat, J.F., Lambert, M., Levieux, G., Villeneuve, N., Froger, J.L., 2009. Gravity structure of Piton de la Fournaise volcano and inferred mass transfer during the 2007 crisis. *J. Volcanol. Geotherm. Res.* 184, 31–48. <https://doi.org/10.1016/j.jvolgeores.2009.01.024>
- Garduño-Monroy, V.H., Saucedo-Girón, R., Jiménez, Z., Gavilanes-Ruiz, J.C., Cortés-Cortés, A., Uribe-Cifuentes, R.M., 1998. La falla tamazula, límite suroriental del bloque jalisco, y sus relaciones con el complejo volcánico de Colima, México. *Rev. Mex. Ciencias Geol.* 15, 132–144.
- Gudmundsson, A., 2011. Deflection of dykes into sills at discontinuities and magma-chamber formation. *Tectonophysics* 500, 50–64.
<https://doi.org/10.1016/j.tecto.2009.10.015>
- Heap, M.J., Baumann, T., Gigli, A., Kolzenburg, S., Ryan, A.G., Villeneuve, M., Russell, J.K., Kennecott, L.A., Rosas-Carbajal, M., Clynne, M.A., 2021. Hydrothermal alteration can result in pore pressurization and volcano instability. *Geology* 49, 1348–1352. <https://doi.org/10.1130/G49063.1>
- Herrmann, R.B., 2010. Computer programs in seismology: An evolving tool for instruction and research. *Seismol. Res. Lett.* 84, 1081–1088.
<https://doi.org/10.1785/0220110096>
- Jaxybulatov, M., Shapiro, N.M., Koulakov, I., Mordret, A., Landes, M., Sens-Schönfelder, C., 2014. A large magmatic sill complex beneath the Toba caldera. *Science (80-.)*. 617. <https://doi.org/10.1126/science.1258582>
- Jay, J.A., Pritchard, M.E., West, M.E., Christensen, D., Haney, M., Minaya, E., Sunagua, M., McNutt, S.R., Zabala, M., 2012. Shallow seismicity, triggered seismicity, and ambient noise tomography at the long-dormant Uturuncu Volcano, Bolivia. *Bull. Volcanol.* 74, 817–837.
<https://doi.org/10.1007/s00445-011-0568-7>
- Kuznetsov, P.Y., Koulakov, I.Y., 2014. The three-dimensional structure beneath the Popocatepetl volcano (Mexico) based on local earthquake seismic tomography. *J. Volcanol. Geotherm. Res.* 276, 10–21.

- <https://doi.org/10.1016/j.jvolgeores.2014.02.017>
- Lecocq, T., Caudron, C., Brenguier, F., 2014. MSNoise, a Python Package for Monitoring Seismic Velocity Changes Using Ambient Seismic Noise. *Seismol. Res. Lett.* 85, 715–726. <https://doi.org/10.1785/0220130073>
- Lee, S.J., Kim, S., Rhie, J., Kang, T.S., Kim, Y.H., 2021. Upper crustal shear wave velocity and radial anisotropy beneath Jeju Island volcanoes from ambient noise tomography. *Geophys. J. Int.* 225, 1332–1348. <https://doi.org/10.1093/gji/ggab026>
- Lerebour, P., Rançon, J.P., Augé, T., 1989. The Grand Brûlé exploration drilling: New data on the deep framework of the Piton de la Fournaise volcano. Part 2: Secondary minerals. *J. Volcanol. Geotherm. Res.* 36, 129–137. [https://doi.org/10.1016/0377-0273\(89\)90001-7](https://doi.org/10.1016/0377-0273(89)90001-7)
- Levshin, A.L., Pisarenco, V.F., Pogrebinsky, G.A., 1972. On a frequency-time analysis of oscillations. *Ann. Geophys.* 28, 211–218.
- Luhr, J.F., 2002. Petrology and geochemistry of the 1991 and 1998–1999 lava flows from Volcán de Colima, México: Implications for the end of the current eruptive cycle. *J. Volcanol. Geotherm. Res.* 117, 169–194. [https://doi.org/10.1016/S0377-0273\(02\)00243-3](https://doi.org/10.1016/S0377-0273(02)00243-3)
- Luhr, J.F., Carmichael, I.S.E., 1980. The Colima Volcanic complex, Mexico - I. Post-caldera andesites from Volcán Colima. *Contrib. to Mineral. Petrol.* 71, 343–372. <https://doi.org/10.1007/BF00374707>
- Luhr, J.F., Nelson, S.A., Allan, J.F., Carmichael, I.S.E., 1985. Active rifting in southwestern Mexico: Manifestations of an incipient eastward spreading-ridge jump. *Geology* 13, 54–57. [https://doi.org/10.1130/0091-7613\(1985\)13<54:ARIS:MM>2.0.CO;2](https://doi.org/10.1130/0091-7613(1985)13<54:ARIS:MM>2.0.CO;2)
- Medina, F., Espindola, J.M., De La Fuente, M., Menai, M., 1996. A gravity model of the Colima, Mexico region. *Geofis. Int.* 35, 409–414. <https://doi.org/10.22201/igeof.00167169p.1996.35.4.533>
- Mendoza-Rosas, A.T., De la Cruz-Reyna, S., 2008. A statistical method linking geological and historical eruption time series for volcanic hazard estimations: Applications to active polygenetic volcanoes. *J. Volcanol. Geotherm. Res.* 176, 277–290. <https://doi.org/10.1016/j.jvolgeores.2008.04.005>
- Michael West, 2006. The Colima Deep Seismic Experiment: Imaging the Magmatic Root of Colima Volcano. https://doi.org/10.7914/SN/ZA_2006
- Mordret, A., Landés, M., Shapiro, N.M., Singh, S.C., Roux, P., 2014a. Ambient noise surface wave tomography to determine the shallow shear velocity structure at Valhall: Depth inversion with a Neighbourhood Algorithm. *Geophys. J. Int.* 198, 1514–1525. <https://doi.org/10.1093/gji/ggu217>

- Mordret, A., Landés, M., Shapiro, N.M., Singh, S.C., Roux, P., Barkved, O.I., 2013. Near-surface study at the valhall oil field from ambient noise surface wave tomography. *Geophys. J. Int.* 193, 1627–1643. <https://doi.org/10.1093/gji/ggt061>
- Mordret, A., Rivet, D., Landés, M., Shapiro, N.M., 2014b. 3-D shear-velocity anisotropic model of Piton de la Fournaise volcano (La Réunion Island) from ambient seismic noise. *J. Geophys. Res. Solid Earth* 120, 406–427. <https://doi.org/10.1002/2014JB011654>
- Moschetti, M.P., Ritzwoller, M.H., Shapiro, N.M., 2007. Surface wave tomography of the western United States from ambient seismic noise: Rayleigh wave group velocity maps. *Geochemistry Geophysics Geosystems* 8, 1–10. <https://doi.org/10.1029/2007GC001654>
- Norini, G., Agliardi, F., Crosta, G., Groppelli, G., Zuccato, M.C., 2019. Structure of the Colima Volcanic Complex: Origin and Behaviour of Active Fault Systems in the Edifice, in: *Active Volcanoes of the World*. Springer Berlin Heidelberg, pp. 27–54. https://doi.org/10.1007/978-3-642-25911-1_8
- Norini, G., Capra, L., Groppelli, G., Agliardi, F., Pola, A., Cortes, A., 2010. Structural architecture of the Colima Volcanic Complex. *J. Geophys. Res. Solid Earth* 115, 1–20. <https://doi.org/10.1029/2010JB007649>
- Núñez-Cornú, F., Nava, F.A., De la Cruz-Reyna, S., Jiménez, Z., Valencia, C., García-Arthur, R., 1994. Seismic activity related to the 1991 eruption of Colima Volcano, Mexico. *Bull. Volcanol.* 56, 228–237. <https://doi.org/10.1007/BF00279608>
- Núñez-Cornú, F.J., Sánchez-Mora, C., 1999. Stress field estimations for Colima volcano, Mexico, based on seismic data. *Bull. Volcanol.* 60, 568–580. <https://doi.org/10.1007/s004450050252>
- Ochoa-Chávez, J.A., Esudero, C.R., Núñez-Cornú, F.J., Bandy, W.L., 2016. P-Wave Velocity Tomography from Local Earthquakes in Western Mexico. *Pure Appl. Geophys.* 173, 3487–3511. <https://doi.org/10.1007/s00024-015-1183-3>
- Pacheco, J.F., Bandy, W., Reyes-Dávila, G.A., Núñez-Cornú, F.J., Ramírez-Vázquez, C.A., Barrón, J.R., 2003. The Colima, Mexico, earthquake (Mw 5.3) of 7 March 2000: Seismic activity along the southern Colima rift. *Bull. Seismol. Soc. Am.* 93, 1458–1467. <https://doi.org/10.1785/0120020193>
- Reubi, O., Blundy, J., Varley, N.R., 2013. Volatiles contents, degassing and crystallisation of intermediate magmas at Volcan de Colima, Mexico, inferred from melt inclusions. *Contrib. to Mineral. Petrol.* 165, 1087–1106. <https://doi.org/10.1007/s00410-013-0849-6>

- Reyes-Dávila, G.A., Arámbula-Mendoza, R., Espinasa-Pereña, R., Pankhurst, M.J., Navarro-Ochoa, C., Savov, I., Vargas-Bracamontes, D.M., Cortés-Cortés, A., Gutiérrez-Martínez, C., Valdés-González, C., Domínguez-Reyes, T., González-Amezcuca, M., Martínez-Fierros, A., Ramírez-Vázquez, C.A., Cárdenas-González, L., Castañeda-Bastida, E., Vázquez Espinoza de los Monteros, D.M., Nieto-Torres, A., Campion, R., Courtois, L., Lee, P.D., 2016. Volcán de Colima dome collapse of July, 2015 and associated pyroclastic density currents. *J. Volcanol. Geotherm. Res.* 320, 100–106. <https://doi.org/10.1016/j.jvolgeores.2016.04.015>
- Ritzwoller, M.H., Levshin, A.L., 1998. Eurasian surface wave tomography: Group velocities. *J. Geophys. Res. Solid Earth* 103, 4829–4878. <https://doi.org/10.1029/97jb02622>
- Robin, C., Mossand, P., Camus, G., Cantagrel, J.M., Gougaud, A., Vincent, P.M., 1987. Eruptive history of the Colima volcanic complex (Mexico). *J. Volcanol. Geotherm. Res.* 31, 99–113. [https://doi.org/10.1016/0377-0273\(87\)90008-4](https://doi.org/10.1016/0377-0273(87)90008-4)
- Rosas-Elguera, J., Ferrari, L., Garduño-Monroy, V.H., Urrutia-Fucugauchi, J., 1996. Continental boundaries of the Jalisco block and their influence in the Pliocene-Quaternary kinematics of western Mexico. *Geology* 24, 921–924. [https://doi.org/10.1130/0091-7613\(1996\)024<0921:CBOTJB>2.3.CO;2](https://doi.org/10.1130/0091-7613(1996)024<0921:CBOTJB>2.3.CO;2)
- Roverato, M., Capra, L., Sulpizio, R., Norini, G., 2011. Stratigraphic reconstruction of two debris avalanche deposits at Colima Volcano (Mexico): Insights into pre-failure conditions and climate influence. *J. Volcanol. Geotherm. Res.* 207, 35–46. <https://doi.org/10.1016/j.jvolgeores.2011.07.003>
- Sambridge, M., 1995. Geophysical inversion with a neighbourhood algorithm-I. Searching a parameter space. *Geophys. J. Int.* 138, 479–494. <https://doi.org/10.1046/j.1365-246X.1999.00876.x>
- Saucedo, R., Macías, J.L., Gavilanes, J.C., Arce, J.L., Komorowski, J.C., Gardner, J.E., Valdez-Moreno, G., 2010. Eyewitness, stratigraphy, chemistry, and eruptive dynamics of the 1913 Plinian eruption of Volcán de Colima, México. *J. Volcanol. Geotherm. Res.* 191, 149–166. <https://doi.org/10.1016/j.jvolgeores.2010.01.011>
- Savov, I.P., Luhr, J.F., Navarro-Ochoa, C., 2008. Petrology and geochemistry of lava and ash erupted from Volcán Colima, Mexico, during 1998-2005. *J. Volcanol. Geotherm. Res.* 174, 241–256. <https://doi.org/10.1016/j.jvolgeores.2008.02.007>
- Schimmel, M., 1999. Phase cross-correlations: Design, comparisons, and applications. *Bull. Seismol. Soc. Am.* 89, 1366–1378.

- Schimmel, M., Gallart, J., 2007. Frequency-dependent phase coherence for noise suppression in seismic array data. *J. Geophys. Res. Solid Earth* 112, 1–14. <https://doi.org/10.1029/2006JB004680>
- Schimmel, M., Paulssen, H., 1997. Noise reduction and detection of weak, coherent signals through phase-weighted stacks. *Geophys. J. Int.* 130, 497–505. <https://doi.org/10.1111/j.1365-246X.1997.tb05664.x>
- Shelly, D.R., Hill, D.P., Massin, F., Farrell, J., Smith, R.B., Taira, T., 2013. A fluid-driven earthquake swarm on the margin of the Yellowstone caldera. *J. Geophys. Res. Solid Earth* 118, 4872–4886. <https://doi.org/10.1002/jgrb.50362>
- Spica, Z., Perton, M., Legrand, D., 2017. Anatomy of the Colima volcano magmatic system, Mexico. *Earth Planet. Sci. Lett.* 459, 1–13. <https://doi.org/10.1016/j.epsl.2016.11.010>
- Sychev, I. V., Koulakov, I., Egorushkin, I., Zhuravlev, S., West, M., El, S., El Khrepy, S., Al-Arifi, N., Alajmi, M.S., Al-Arifi, N., Alajmi, M.S., 2019. Fault-Associated Magma Conduits Beneath Volcán de Colima Revealed by Seismic Velocity and Attenuation Tomography Studies. *J. Geophys. Res. Solid Earth* 124, 8908–8923. <https://doi.org/10.1029/2019JB017449>
- Wang, Y., Lin, F.C., Schmandt, B., Farrell, J., 2017. Ambient noise tomography across Mount St. Helens using a dense seismic array. *J. Geophys. Res. Solid Earth* 122, 4492–4508. <https://doi.org/10.1002/2016JB013769>
- Xie, J., Ritzwoller, M.H., Shen, M., Yang, Y., Zheng, Y., Zhou, L., 2013. Crustal radial anisotropy across eastern Tibet and the Western Yangtze Craton. *J. Geophys. Res. Solid Earth* 118, 4226–4252. <https://doi.org/10.1002/jgrb.50296>
- Yang, T., Grand, S.P., Wilson, D., Guzman-Speziale, M., Gomez-Gonzalez, J.M., Dominguez-Reyes, T., Ni, J., 2009. Seismic structure beneath the Rivera subduction zone from finite-frequency seismic tomography. *J. Geophys. Res. Solid Earth* 114, 1–12. <https://doi.org/10.1029/2008JB005830>
- Zobin, V.M., Luhr, J.F., Taran, Y.A., Bretón, M., Cortés, A., De La Cruz-Reyna, S., Domínguez, T., Galindo, I., Gavilanes, J.C., Muñíz, J.J., Navarro, C., Ramírez, J.J., Reyes, G.A., Ursúa, M., Velasco, J., Alatorre, E., Santiago, H., 2002. Overview of the 1997-2000 activity of Volcán de Colima, México. *J. Volcanol. Geotherm. Res.* 117, 1–19. [https://doi.org/10.1016/S0377-0273\(02\)00232-9](https://doi.org/10.1016/S0377-0273(02)00232-9)

Journal Pre-proof

CRediT author statement

Raphael S.M. De Plaen: Conceptualization, Investigation, Visualization, Writing - Review & Editing, Formal analysis. **Aurélien Mordret:** Supervision, Methodology, Software, Investigation. **Raul Arámbula-Mendoza:** Supervision, Data curation, Writing – original draft. **Dulce Vargas-Bracamontes:** Supervision, Data curation, Writing – original draft. **Victor Hugo Márquez-Ramírez:** Supervision, Project administration, Funding acquisition, Writing – original draft, Resources. **Thomas Lecocq:** Supervision, Software. **Carlos Ariel Ramírez Vázquez:** Data Curation. **Miguel González Amézquita:** Data Curation

Declaration of interests

The authors declare that they have no known competing financial interests or personal relationships that could have appeared to influence the work reported in this paper.

The authors declare the following financial interests/personal relationships which may be considered as potential competing interests:

Journal Pre-proof

Highlights

We built the highest-resolution anisotropic shear wave velocity models to date of Volcán de Colima

A distinct high-velocity anomaly under Nevado de Colima highlights the distinction between the former, now solidified, system

We observe a network of deeply rooted NE-SW oriented low velocity zones, parallel to the Tamazula fault

The negative radial anisotropy indicates that magma under Volcán de Colima follows vertically oriented structures such as dikes and cracks